Exciton polaritons reveal “hidden” populations in functionalized pentacene films

J. D. B. Van Schenck[1], W. Goldthwaite[1], R. Puro[1], J. E. Anthony[2], and O. Ostroverkhova[1]

[1]Department of Physics, Oregon State University, Corvallis, OR 97331
[2]Center for Applied Energy Research, University of Kentucky, Lexington, KY 40511

ABSTRACT

We present a systematic investigation of strong exciton-photon coupling in functionalized pentacene (TIPS–Pn)-based films in all-metal cavities, depending on molecular concentration and film morphology. The Rabi splittings of up to 270 meV are observed, with the highest values achieved in pristine amorphous TIPS–Pn films. The exciton-photon interaction strength for the lowest-energy (0–0) exciton scaled with the square root of the molecular density, which was independent of whether the long-range molecular order was present in films. The molecular populations in the disordered regions of the films coupled to the cavity most strongly in all films, including pristine crystalline films. Such populations, with molecular configurations favoring interaction with the cavity electromagnetic field, were not readily identifiable in optical absorption spectra of bare (i.e. not coupled to the cavity) films, which highlights the capability of polariton spectroscopy to reveal these molecular ensembles, which are “hidden” in polycrystalline films. The linear scaling of the exciton-photon interaction strength with the square root of the oscillator strengths was observed in dilute TIPS–Pn:PMMA films but not in pristine TIPS–Pn films, either amorphous or crystalline. In particular, in pristine films, the exciton-photon interaction strength for the vibrational (0–m, $m > 0$) excitons was higher than expected based on the oscillator strengths extracted from the optical spectra of bare films, which was attributed to enhanced exciton delocalization facilitated by the 2D brickwork motif of TIPS–Pn. Similar observations were made in functionalized anthradithiophene (diF TES–ADT) films (also exhibiting a 2D brickwork packing motif), but not in TIPS–Tc films which suggests that the underlying mechanisms rely on short-range intermolecular interactions determined by the molecular packing motif and resulting nanomorphology.

1 Introduction

Organic (opto)electronic and photonic materials have attracted attention due to their low cost, solution processability, and tunable properties. [1] A broad range of (opto)electronic and photonic applications, including organic light-emitting diodes (OLEDs), photovoltaics (OPVs), sensors, photorefractive three-dimensional displays, lasers, has been demonstrated, and many of them commercialized. [1, 2] One of the areas that has experienced recent dramatic growth is research into strong coupling between organic molecules and resonant structures, such as microcavities, [3, 4] plasmonic nanostructures, [5] or hyperbolic metamaterials, [6] and associated physics and applications of this phenomenon. The complexity of interactions involved in the strong coupling and how they translate into properties of light-matter hybrid states (polaritons) have inspired theoretical effort [7–10] and enabled experimental demonstrations of Bose-Einstein Condensation and associated exciting phenomena including polaritonic lasing, [11–13] nonlinear amplification, [14] and superfluidity. [15]

Additionally, it has been of considerable interest to understand how the strong coupling, and resulting light-matter hybrid polariton states, may contribute to the performance of organic (opto)electronic devices. [16–20] For example, exciton polaritons in organic photodiodes incorporated into microcavities enhanced the device responsivity by extending the photodiode sensitivity to wavelengths beyond those achievable in the absence of strong coupling. [17] In a planar OPV incorporated in a resonant cavity, strong coupling-modified optical absorption enabled reduction in the losses. [20] In perylene diimide field-effect transistors on plasmonic nanostructures, an order of magnitude enhancement in charge carrier mobility was observed and attributed to an enhanced carrier delocalization promoted by hybrid states. [21] On the other hand, charge carrier mobilities in organic transistors based on donor-acceptor copolymers or phthalocyanines incorporated in resonant cavities were similar to those in control devices without the cavity structures. [22, 23] Therefore, more work is needed to understand the polariton properties in organic semiconductors, their contribution to characteristics of organic (opto)electronic devices, and underlying mechanisms that determine (opto)electronic properties.

Over the past decade, strong coupling has been demonstrated in a variety of organic materials, expanding the library of polaritonic materials well beyond traditional organic polaritonic systems involving J-aggregates dispersed in polymer films or gels. [24] This includes materials that have been previously explored for (opto)electronic applications. Examples are photorefractive glasses such as a dicyanomethylenedihydrofuran derivative (exhibiting ultrastrong coupling with Rabi splitting of $> 1\ eV$), [25] OLED and OPV materials such as 4,4-cyclohexylidenebis[N,N-bis(4-methylphenyl)benzenamine] (TAPC) [26] and phthalocyanines, [17] and OFET materials such as derivatives of acenes (e.g. anthracene (Ac), tetracene (Tc), pentacene (Pn)) [27–30, 32] and of anthradithiophenes (ADTs). [31] In addition to their attractive electronic properties, acenes and ADTs have served as model systems for photophysical studies on all levels, from single molecules incorporated in solids, [33–37] which began from seminal demonstration of optical detection of single pentacene (Pn) molecules dispersed in a p-terphenyl crystal, [33] to molecular crystals. [38–40, 42] Many of these derivatives (including Tc, Pn, and ADT) exhibit singlet fission (SF), a process of creating two triplet excitons upon excitation of a singlet state, which has generated a considerable amount of attention due to its potential to enhance the efficiency of organic solar cells. [41]

One representative benchmark electronic and SF material of this class is Pn functionalized with TIPS side groups (TIPS–Pn). [43] In FETs, TIPS–Pn exhibits hole mobilities of $> 1\ cm^2/(Vs)$ and up to 11 $cm^2/(Vs)$, depending on the crystal polymorph and/or film crystallinity and morphology. [1, 44] These are among the highest mobilities in solution-processable OFETs, which has motivated research into mechanisms responsible for its enhanced electronic characteristics and into structure-property relationships over the past 20 years. [39, 44–49] In terms of photophysics, TIPS–Pn films exhibit ultrafast ($< 100\ fs$) SF, depending on film morphology, [50, 51, 55] and this process in TIPS–Pn has been extensively studied from the fundamental photophysics standpoint [52, 54, 56] and towards applications in SF-based photovoltaics. [53] Although photophysical and electronic properties of TIPS–Pn have been extensively studied, exploration of properties of polaritons in TIPS–Pn is at its inception, [32, 57] and understanding of how the underlying photophysics of TIPS–Pn and specifics of its film morphology determines these properties has not yet been developed. Such understanding, however, would be important for designing materials for next-generation organic electronic devices utilizing properties of polaritons, which motivates our present study.

In this paper, we investigate strong coupling of excitons in TIPS–Pn-based films of varying TIPS–Pn concentration and morphology, to cavity photons in all-metal microcavities. Inspired by the capability of single molecule spectroscopy to reveal “hidden” molecular populations in ensembles masked by ensemble averaging, [58] we demonstrate how polariton spectroscopy identifies “hidden” populations that couple to the microcavity. Existence of these populations is not readily observed with optical spectroscopy, yet they are important for polaritonic devices. We observe preferential cavity-coupling of TIPS–Pn molecules in the amorphous over the crystalline phase in heterogeneous (mixed-phase) films and in the defect-rich regions in the crystalline phase. We establish that the scaling of the exciton-photon interaction strength for the vibrationless (0-0) exciton with the square root of the molecular density is independent of film crystallinity and morphology. In contrast, the scaling of the interaction strength for the vibrational excitons with the square root of the oscillator strengths depends on the molecular density and breaks down for highly concentrated TIPS–Pn films, which we relate to nanomorphology and associated with it degree of vibrational exciton delocalization.

2 Methods

2.1 Sample Preparation

The microcavities were fabricated using the following procedure: first, a 45 nm silver (Ag) layer was deposited onto a glass (BK7) substrate via thermal evaporation, then a film was spin cast to form the active layer with a thickness of $\sim 100-200$ nm (to create resonant $\lambda/2$ cavities), and finally another 45 nm Ag layer was evaporated on top of the film to finish the cavity. This top Ag layer was masked to only cover a portion of the total substrate, allowing part of the active layer of the same sample to be measured in both "coupled" (that is, contained in the cavity) and "uncoupled" (that is, with no top mirror) states. Regions without (with) the top Ag layer are referred to as "bare film" ("cavity").

Various types of TIPS–Pn films were used as the active layer in the microcavities as schematically shown in Fig. 1, classified as "blends" and "pristine". In the case of blends, TIPS–Pn molecules were embedded in a polymer matrix of poly(methyl methacrylate) (PMMA) at several TIPS–Pn concentrations. For this, TIPS–Pn and PMMA were dissolved in toluene at varying relative concentrations to control the relative density of TIPS–Pn molecules in the resulting film such that the average TIPS–Pn molecular spacing is between $d = 1$ nm and $d = 2$ nm. Calculations of relative concentrations and the resulting average molecular spacings can be found in the SI. [31, 63] For example, concentrations of 13 mM of TIPS–Pn with 40 mg/mL of PMMA and 53 mM of TIPS–Pn with 20 mg/mL of PMMA were used to achieve an average TIPS–Pn molecular spacing of $d = 2$ nm and $d = 1$ nm, respectively. Films were deposited at spin casting speeds between 800 RPM and 3000 RPM. These films are referred to as $F_d^{(B)}$, where the superscript B indicates the film is a blend and the subscript denotes the average TIPS–Pn molecular spacing in nanometers (e.g. $F_2^{(B)}$ and $F_1^{(B)}$ in Fig. 1). The absorbance of selected bare films of these blends is shown in Fig. 2.

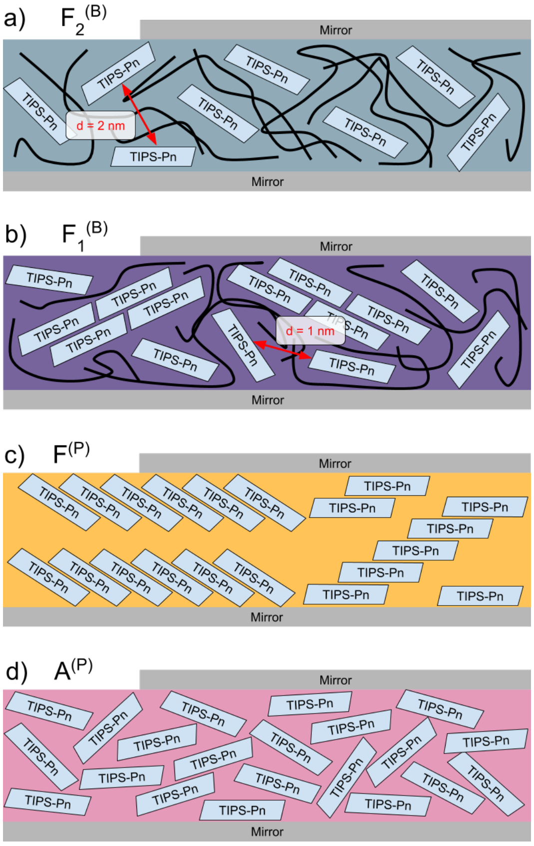

Figure 1: Schematic representations of the morphology in four film types embedded in an optical cavity. (a) Film $F_2^{(B)}$ has TIPS–Pn embedded in a PMMA matrix with average molecular spacing (d) of 2 nm. (b) Film $F_1^{(B)}$ has both amorphous phase TIPS–Pn and crystallites (ordered aggregates) embedded in a PMMA matrix. The average molecular spacing (d) is 1 nm. (c) Film $F^{(P)}$ is a polycrystalline film with the dominant orientation $(00l)$ (for $l = 1, 2, 3$), with the long c-axis of the crystal in the substrate normal direction which is represented on the left of the cavity, with the minor population with (011) orientation schematically represented on the right. (d) Film $A^{(P)}$ is an annealed pristine film where TIPS–Pn molecules are in the amorphous phase.

The "pristine" TIPS–Pn films contained only TIPS–Pn molecules (no PMMA) and were deposited using a 50 mM solution of TIPS–Pn in toluene via spin casting. To improve the film quality, the Ag surface was treated with a 30 mM solution of pentafluorobenzenethiol (PFBT) in ethanol (as described in previous publications [31,65]). The pristine TIPS–Pn films obtained using this deposition method are polycrystalline as confirmed by x-ray diffraction (XRD), and they exhibit $(00l)$ ($l = 1, 2, 3$) and (011) orientations of TIPS–Pn (Fig. S1). [49] These films are referred as $F^{(P)}$ where the superscript P indicates the film is pristine.

To force polycrystalline films into an amorphous state, thermal annealing was employed. Details of this process can be found in the SI and Fig. S2. Briefly, after spin casting, films were placed on a hot plate and held at 250 °C for 20 seconds, allowing the film to fully convert into an amorphous phase as confirmed by the XRD (Fig. S1). These films are referred to as $A^{(P)}$ where the A indicates that the film has been annealed and is amorphous. The absorbance of both the amorphous and crystalline pristine bare films is shown in Fig. 2.

2.2 Optical Characterization

The solution absorption spectrum was measured in a 30 μM solution of TIPS–Pn in toluene placed in a 1 cm fused silica cuvette using a tungsten lamp (Ocean Optics LS-1) and a fiber-coupled spectrometer (Ocean Optics USB2000). The spectrum was fit using a vibronic progression model: [38]

$$\frac{A(\hbar\omega)}{\hbar\omega} = A_0 \sum_{m=0}^{4} \frac{e^{-S}S^m}{m!} \Gamma_{\sigma_{00}(1+m\Delta\sigma)}(\hbar\omega - E_X - mE_V) \tag{1}$$

where $A/\hbar\omega$ is the reduced absorption, A_0 is a normalization constant, S is the Huang-Rhys factor, Γ_σ is a normalized Lorentzian lineshape with half width at half maximum (HWHM) of σ which incorporates σ_{00} (the HWHM of the 0-0 peak) and $\Delta\sigma$ (a progressive broadening term). [59] Finally, E_X is the 0-0 exciton energy and E_V is the vibrational energy quantum. The fit and associated parameter values are given in Fig. S4 and Table 1.

The microcavities were characterized using angle resolved reflectance on a custom-built optical assembly. White light from a fiber-coupled tungsten filament source (Ocean Optics LS-1) was passed through a linear polarizer to select either s- or p-polarizations before being focused onto the sample at angles of incidence ranging from 15° to 80° in steps of 5°. Reflected light was then collected and analyzed with an Ocean Optics USB2000 spectrometer.

The absorbance for each bare film was measured using the reflectance of that film at low angle of incidence (15°). In particular, the reduced absorption spectra were modeled as:

$$A_{red}(\hbar\omega) = -\frac{1}{\hbar\omega}\log_{10}(R_c) = \sum_i A_i \Gamma_{\sigma_i}\left(\hbar\omega - E_X^{(0i)}\right) \tag{2}$$

where A_{red} is the reduced absorption, $\hbar\omega$ is the incident photon energy, R_c is the reflectance corrected for the plasma frequency the silver substrate of the film, A_i is the area of the i^{th} reduced absorbance resonance, Γ_{σ_i} is a normalized Lorentzian (Gaussian) lineshape with HWWM (standard deviation) of σ_i and $E_X^{(0i)}$ is the resonance (exciton) energy.

In the case of films $F_2^{(B)}$ and $A^{(P)}$, in addition to the general model of Eq. (2), the data were fit with the more specific vibronic progression (eq 1). Figures S5 and S8 show examples of the fits; fit parameters are summarized in Table 1. To characterize the blends with contributions of amorphous and crystalline phases to the optical absorption (e.g.$F_{1.3}^{(B)}$ in Fig. S6), the absorption spectrum was fit to determine the relative contribution of these phases to the overall absorption. The amorphous phase contribution to the spectrum was modeled as a vibronic progression (eq 1) with the $E_X^{(00)}$ energy fixed to 1.91 eV, and the crystalline phase contribution was modeled using four Gaussian functions fixed at the center energies of the peaks obtained from analysis of the $F_1^{(B)}$ spectrum. Fit parameters are included in Table S2.

The angle resolved reflectance of the cavities where modeled using the following equation to extract the center energies of each feature:

$$R(\hbar\omega,\theta) = BS(\hbar\omega,\theta) + \sum_n C_n(\theta)\Gamma_{G_n(\theta)}(\hbar\omega - E_n(\theta)) \tag{3}$$

where R is the reflectance at photon energy $\hbar\omega$ and angle of incidence θ, BS is a baseline reflectance due to the silver substrate, and the resonances in the spectra are modeled with either a Lorentzian or Gaussian lineshape (Γ) depending on the film morphology. $C_n(\theta)$ is the area, $G_n(\theta)$ is the half-width at the half maximum for Lorentzian lineshapes and the standard deviation for Gaussian lineshapes and $E_n(\theta)$ is the center energy for the n^{th} resonance at angle of incidence θ.

The photoluminescence (PL) spectra of the bare films were measured by exciting the samples with a continuous wave 532 nm frequency-doubled $Nd:YVO_4$ laser (Verdi-5, Coherent, Inc.)

and collecting the emitted light with an Ocean Optics USB2000-FLG spectrometer. [38] The PL spectra of select films are shown in Fig. S10. The PL lifetimes were measured using a 532 nm pulsed excitation from a frequency doubled Nd:YAG laser (NE Fianium-1060), and the emitted photons were collected using a PDM Series SPAD and a time-correlated single-photon counting card (TimeHarp 200, Picoquant, Inc.). The measurements were limited by an instrument response function to a resolution of 380 ps.

2.3 Numerical Analysis

The center energies of the cavity reflection resonances were modeled using a coupled oscillators model for polaritons: [31]

$$H = \begin{bmatrix} E_{ph}(\theta) & V_{00} & V_{01} & V_{02} & \cdots \\ V_{00} & E_X^{(00)} & 0 & 0 & \cdots \\ V_{01} & 0 & E_X^{(01)} & 0 & \cdots \\ V_{02} & 0 & 0 & E_X^{(02)} & \cdots \\ \vdots & \vdots & \vdots & \vdots & \ddots \end{bmatrix} \tag{4}$$

where $E_{ph}(\theta)$ is the cavity photon energy at angle of incidence θ, $E_X^{(0i)}$ is the energy of the i^{th} exciton and V_{0i} is the corresponding interaction energy. The number of excitons included in the matrix depends upon the film, see Table S6 for details. The cavity photon E_{ph} is modeled with:

$$E_{ph}(\theta) = E_0 \left(1 - \left(\frac{\sin(\theta)}{n_{eff}}\right)^2\right)^{-\frac{1}{2}} \tag{5}$$

where E_0 is the cavity photon energy at normal incidence and n_{eff} is the effective refractive index. The Hamiltonian was numerically diagonalized at each angle of incidence to obtain the polariton branch energies which were then compared to the center energies $E_n(\theta)$ in a nonlinear least squares optimization to determine the interaction strengths V_{0m}. All fit parameters are given in Tables 1 and S6.

Next, the exciton-photon interaction strength was considered to be in the following form: [60]

$$V = \frac{\hbar\Omega}{2} = \mu\sqrt{\frac{N_0\hbar\omega}{2\epsilon\mathcal{V}_{\text{mode}}}} \tag{6}$$

where V is the interaction energy, $\hbar\Omega$ is the Rabi splitting, μ is the transition dipole moment of the molecules coupled to the cavity, N_0 is the number of coupled molecules inside the photon mode volume $\mathcal{V}_{\text{mode}}$, $\hbar\omega$ is the photon energy and ϵ is the dielectric constant of the cavity-filling material. Of particular relevance here is that this predicts that $V \propto \mu \propto \sqrt{f}$ where f is the oscillator strength of molecule's absorptive transition.

As a result, the interaction strengths $2V_{0m}$ (Rabi splitting) for each film were modeled with a linear fit: [31]

$$2V_{0m} = A \cdot \sqrt{f_{0m}/f_{00}} + B \tag{7}$$

where f_{0m} is the oscillator strength of the m^{th} exciton, extracted from bare film fits. Although eq 6 predicts that the interaction strength scales with the transition dipole moment (equivalently the root of the oscillator strength), it has been shown [31] that this proportionality is not always accurate for molecular aggregates, due to intermolecular effects not accounted for by eq 6. To address this, the linear model (eq 7) is applied in two forms. For TIPS–Pn:PMMA films, B is fixed at zero reducing the model to the expected proportionality. For pristine TIPS–Pn films, A is fixed at zero reducing the model to a constant fit. Figure 6(a) shows these fits, and the parameter values are given in Table S7.

Finally, the lowest-energy (0-0) exciton-photon interaction energies $2V_{00}$ were also fit using a proportional model with the square root of the molecular density, estimated using the molecular volume $\mathcal{V}$. The SI provides a detailed description of how these volumes were calculated; briefly, for TIPS–Pn:PMMA films, the average molecular spacing was used:

$$\mathcal{V}_{F_d^{(B)}} = \frac{4}{3}\pi\left(\frac{d}{2}\right)^3 \tag{8}$$

whereas for pristine crystalline films the geometric mean of the lattice constants was used:

$$\mathcal{V}_{F^{(P)}} = \sqrt[3]{abc} \tag{9}$$

with $a = 0.75650\ nm,\ b = 0.77500\ nm,\ c = 1.6835\ nm$ [49]. Finally for the pristine amorphous films, the volume was calculated from the thickness contraction experienced by films during the annealing process used for fabrication of amorphous films ($\mathcal{V}_{A^{(P)}} = (0.75 \pm 0.15)\mathcal{V}_{F^{(P)}}$, see Sec. 2.1 and Figs. S2 and S3). So, the interaction energies $2V_{00}$ were fit according to:

$$2V_{00} = C \cdot \sqrt{\frac{1}{\mathcal{V}}} \tag{10}$$

with fit parameters given in Table S8.

3 Results

3.1 Optical properties of bare films

Figure 2 shows absorption spectra of various types of bare TIPS–Pn:PMMA and pristine TIPS–Pn films used in our studies, schematically depicted in Fig. 1, as well as that of TIPS–Pn in dilute toluene solution. The spectrum in dilute solution shows the characteristic vibronic progression expected for non-interacting TIPS–Pn molecules (Fig. S4), with the 0-0 energy of 1.926 eV and a Huang-Rhys (HR) factor of $S = 0.74$ due to coupling to a C-C stretching mode at 0.164 eV. The HWHM of the 0-0 peak σ_{00} was only 25 meV though the progressive broadening $\Delta\sigma$ was large (0.67) indicating that the exciton is coupled to a distribution of C-C stretching modes centered on 0.164 eV (Table 1). [59]

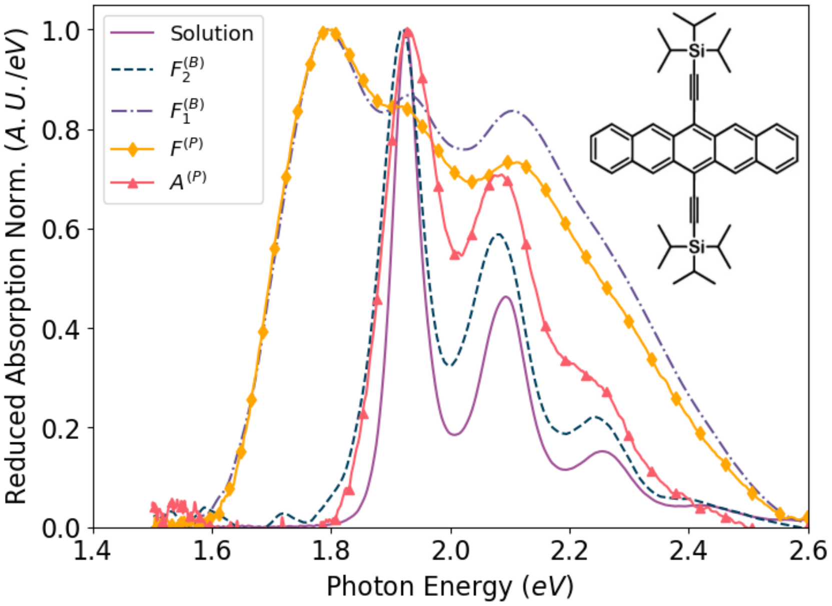

Figure 2: The reduced absorption (normalized to the 0-0 peak height) from four TIPS–Pn films deposited onto a silver substrate: film $F_2^{(B)}$ (dashed), film $F_1^{(B)}$ (dash–dotted), film $F^{(P)}$ (diamonds), and film $A^{(P)}$ (triangles). The reduced absorption spectrum from TIPS–Pn in dilute (30 μM) solution in toluene is also shown (solid) for comparison. The $F_2^{(B)}$ and $A^{(P)}$ films show an amorphous phase response, with a 0–0 transition energy of ~1.9 eV, which is similar to that of dilute solution. Both the $F_1^{(B)}$ and $F^{(P)}$ films show a crystalline phase response, with a 0–0 transition energy of ~1.8 eV. The inset shows the molecular structure of TIPS–Pn.

The dilute TIPS–Pn:PMMA blend $F_2^{(B)}$ exhibited spectra similar to that of dilute solution, which were also modeled with a vibronic progression (Fig. S5). The 0-0 energy in $F_2^{(B)}$ is at 1.916 eV (10 meV lower than in solution, due to differences in the dielectric environment), and the vibronic progression shows coupling to a C-C stretching mode at 0.162 eV with the HR factor of $S = 0.72$. The 0-0 HWHM σ_{00} is 36 meV (slightly larger than that in solution), but the progressive broadening $\Delta\sigma$ is only 0.31, less than half of that in solution. This is indicative of the PMMA environment imposing restrictions on the molecular vibrational degrees of freedom, decreasing the width of the distribution of the C-C stretching modes that the exciton can couple to (decreasing $\Delta\sigma$) while also presenting a more inhomogeneous local environment for the molecules (increasing σ_{00}).

In contrast, spectra of the more concentrated TIPS–Pn:PMMA blend $F_1^{(B)}$ featured a ~0.14 eV (~50 nm) red shift of the 0-0 energy (1.78 eV) and significant peak broadening, features similar to those in pristine polycrystalline TIPS–Pn films $F^{(P)}$ (Figs.2, S7, and S9). These spectral changes are due to intermolecular interactions, and they are consistent with previous studies of TIPS–Pn films and single crystals. [48, 55, 56, 61, 62] For example, the 0–0 red shifts of $45 - 70$ nm in polycrystalline TIPS–Pn films have been previously observed depending on morphology, [48] and the large 0–0 solution-crystal red shifts in TIPS–Pn crystals were attributed to efficient mixing of the Frenkel and charge transfer (CT) states. [62] Furthermore, the GW/BSE calculations confirmed that the lowest-energy exciton in crystalline TIPS–Pn possesses a CT character and is delocalized over ~3 nm in the a-b plane of the crystal. [56] The development of this phase (which will be referred to as "‘crystalline"’, as the emergence of the low-energy 1.78 eV peak in the optical absorption spectra strongly correlates with the emergence of crystalline structure detected by the XRD) in concentrated blends, with the pronounced effects of TIPS–Pn intermolecular interactions on the optical absorption spectra, can be seen in the spectra of blends $F_d^{(B)}$ with $1 < d < 2$. For example, in the optical spectrum of a TIPS–Pn:PMMA film $F_{1.3}^{(B)}$ (Fig. S6), both the crystalline and amorphous (that is having the optical absorption spectra similar to those of dilute blends and amorphous films $A^{(P)}$, Fig. 2) contributions could be identified, constituting 64% and 36%, respectively, of the total oscillator strength. Similar concentration-dependent evolution of spectral features has also been observed in films of anthradithiophene (ADT) derivatives such as a benchmark organic semiconductor material diF TES-ADT, [38, 63] blended with PMMA at various concentrations. The diF TES-ADT exhibits similar to TIPS–Pn trends in polariton behavior, which will be discussed in Sec. 4 to highlight that the observations presented here for TIPS–Pn represent a general trend for a particular class of functionalized acenes and ADTs.

The pristine TIPS–Pn amorphous films $A^{(P)}$ had absorption spectra with features considerably more similar to those of dilute TIPS–Pn:PMMA blends (such as $F_2^{(B)}$) than to those in the polycrystalline films $F^{(P)}$, in agreement with previous work (Fig. S8). [48] In particular, the 0-m peak energies in the S_0-S_1 manifold were close to those in dilute blends and solutions. However, the 0-m peak ratios and the peak widths were different from those in dilute blends (Table 1) which suggests that intermolecular interactions are not negligible in these films [64] even though the lowest-energy exciton does not show spectral signatures of Frenkel-CT mixing and delocalization in these amorphous films $A^{(P)}$.

The PL measurements reveal additional insights into the photophysics of films under study. In particular, in TIPS–Pn:PMMA blends $F_2^{(B)}$ and $F_{1.3}^{(B)}$, and in pristine amorphous films $A^{(P)}$, the PL spectra were similar (Fig. S10), exhibiting the 0-0 energy close to that in dilute solutions and a vibronic progression. However, the PL yield was considerably different, with the dilute blend $F_2^{(B)}$ exhibiting about a factor of ~20 stronger PL than the amorphous pristine film $A^{(P)}$ under the same excitation conditions. Additionally, considerable shortening of the PL lifetimes was observed as the TIPS–Pn concentration increased (Fig. S11 and Table S5), with the bi-exponential dynamics in all films as compared to the monoexponential 13.8 ns decay in solution. For example, in the amorphous pristine film $A^{(P)}$, PL lifetimes of 0.6 ns and 3.0 ns were obtained, as compared to 1.4 ns and 5.2 ns in the dilute TIPS-Pn:PMMA blend $F_2^{(B)}$, which indicates higher availability of nonradiative decay pathways in pristine films. The PL yield dramatically decreased with the appearance of the 1.78 eV exciton in the optical absorption spectra, and so the PL in pristine crystalline films $F^{(P)}$ was more than two orders of magnitude weaker than that in dilute blends $F_2^{(B)}$. The concentration-dependent evolution of PL properties is due to a combination of enhanced exciton diffusion, enabling nonradiative decay pathways, and an onset of singlet fission which is more efficient in more concentrated and, especially, crystalline phases of TIPS–Pn. [55] Therefore, the PL emission in TIPS–Pn films largely originates from molecules which are in configurations not conducive to singlet fission, either due to a large spatial separation or due to unfavorable molecular orientations.

3.2 Optical properties of films in microcavities

Figures 3, 4 and 5 illustrate optical properties of films discussed above placed in microcavities. All films reveal formation of light-matter hybrid states (exciton polaritons), exhibiting dispersive characteristics observed in the angle-dependent reflectance spectra (e.g. Fig. 3(a) and Fig. 4(a)). The exciton-photon coupling strengths were obtained using a coupled oscillator model as described in Section 2.3 and our previous publication. [31] The interaction strengths for the lowest-energy exciton (referred to as "'0-0"') that couples to the cavity photon obtained in all films are summarized in Tables 1 and S6, featuring the Rabi splitting values ($\hbar\Omega_{00} = 2V_{00}$) between 85 meV in the dilute TIPS–Pn:PMMA films $F_2^{(B)}$ and 253 meV in pristine amorphous TIPS–Pn films $A^{(P)}$ for s-polarized light. In each film, coupling of at least three transitions ($0 - m$ for $m = 0, 1, 2$) to the cavity photon was observed for s-polarized light (Fig. 3(b), Fig. 4(b) and Fig. 5), whereas in p-polarization, coupling to only two exciton transitions could

System	$E_X^{00}(bare)$	E_V	S	σ_{00}	$\Delta\sigma$	$E_X^{00}(cav)$	$2V_{00}$
solution	$1.93\ eV$	$0.16\ eV$	0.72	$25\ meV$	0.67	–	–
$F_2^{(B)}$	$1.92\ eV$	$0.16\ eV$	0.74	$36\ meV$	0.31	$1.91\ eV$	$85\ meV$
$F_1^{(B)}$	$1.79\ eV*$	–	–	$74\ meV*$	–	$1.91\ eV$	$228\ meV$
$A^{(P)}$	$1.93\ eV$	$0.15\ eV$	0.85	$44\ meV$	0.33	$1.93\ eV$	$253\ meV$
$F^{(P)}$	$1.77\ eV*$	–	–	$65\ meV*$	–	$1.73\ eV$	$210\ meV$

Table 1: Exciton and polariton properties in bare films and cavities. The 0–0 exciton energies $\left(\left(E_X^{00}(bare)\right)\right)$, vibrational energy (E_V), Huang-Rhys parameter (S), HWHM of the 0–0 line (σ_{00}), and line broadening $(\Delta\sigma)$ obtained from fits to the absorption spectra of bare films and solution with a vibronic progression with Lorentzian lineshapes (Eq.(1)). *In $F_1^{(B)}$ and $F^{(P)}$, data were fitted with a set of four Gaussian functions in Eq.(2); the 0–0 energy and a standard deviation are included in the table for these films; full list of parameter values can be found in Tables S3 and S4. Also included are the 0–0 exciton energy $\left(E_X^{00}(cav)\right)$ for the population that couples to the cavity and interaction strengths $(2V_{00})$ associated with the s-polarized polaritons in representative cavities containing $F_2^{(B)}$, $F_1^{(B)}$, $F^{(P)}$ and $A^{(P)}$ extracted from fits utilizing equation 4. A full list of cavity parameter values are given in Table S6.

be resolved in most films. Interaction strengths for each transition for all cavities studied are summarized in Table S6.

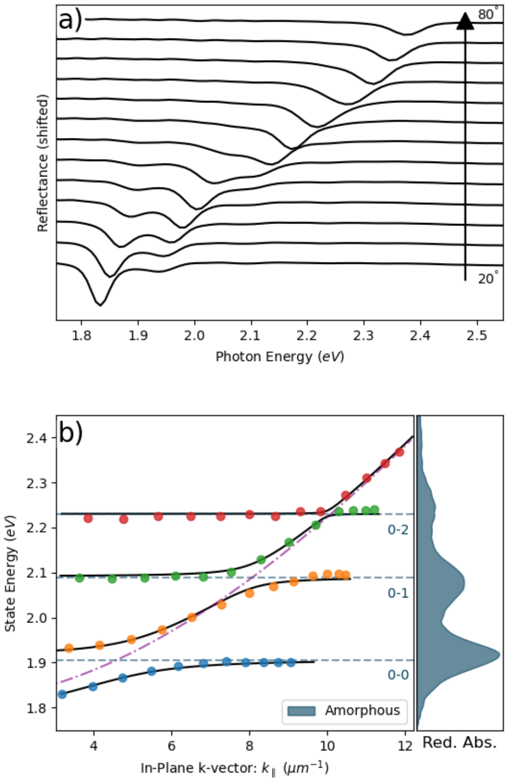

Figure 3: (a) The reflectance from a cavity containing the film $F_2^{(B)}$ at angles of incidence ranging from 20° to 80°. (b) A dispersion plot of the polariton energies extracted from the reflectance. Dots show the experimentally extracted energies, the semi-dashed line shows the photon energy, the dashed line shows the exciton energies for the "amorphous" phase and solid black lines show fits according to the coupled oscillator model. On the right side of (b), the reduced absorption from the corresponding bare film is included for comparison.

The microcavity containing a dilute TIPS–Pn:PMMA film $F_2^{(B)}$ exhibited coupling strengths for the $0-m$ ($m=0,1,2$) transitions of 85 meV, 62 meV, 16 meV (in the s-polarization, Table S6) which scaled well with the square root of the oscillator strength, obtained from fits of the corresponding bare film absorption spectrum with a vibronic progression (Fig. S5), predicted by equation 6 (Fig. 6(a)). The more concentrated blends TIPS–Pn:PMMA $F_{1.3}^{(B)}$ and $F_1^{(B)}$ reveal interesting behavior. Although the absorption spectrum in bare films of this type was dominated in $F_1^{(B)}$ and $F_{1.3}^{(B)}$ by the spectral features of the crystalline phase (Figs. 2 and S6), the coupling to the cavity occurred for exciton transitions corresponding to those of amorphous phase rather than to those of crystalline phase (Fig. 4(b) and Fig. S12). Figure Fig. 4(b) illustrates this preferential coupling for the $F_1^{(B)}$ by showing absorption spectra of the bare film $F_1^{(B)}$ (dominated by those of the crystalline phase) and of bare film $F_2^{(B)}$ (dominated by those of the amorphous phase), side by side with the dispersion characteristics of various polariton branches in $F_1^{(B)}$ cavities. The obtained interaction strengths $2V_{0m}$ (228 meV, 182 meV, 121 meV for 0-0, 0-1, and 0-2 transitions, respectively, in s-polarization) scale well with the square root of oscillator strength f_{0m} (Fig. 6(a)) for the amorphous phase. Additionally, the value of $2V_{00}=228$ meV for $F_1^{(B)}$ is about 2.7 times larger than $2V_{00}=85$ meV in $F_2^{(B)}$ (as expected from the increased molecular density N_{tot} in $F_1^{(B)}$ over $F_2^{(B)}$ and $2V_{00}\propto\sqrt{N_{tot}}$ scaling) by a factor of $\sqrt{(2/1)^3}\approx 2.8$ (Fig. 6(b)). This is interesting since the amorphous phase in the concentrated TIPS–Pn:PMMA blend $F_1^{(B)}$ was not readily apparent in the absorption spectra of the corresponding bare films (Fig. 2).

In contrast to concentrated TIPS–Pn:PMMA blends such as $F_1^{(B)}$, in pristine films the cavity photon coupled to the expected molecular transitions. In particular, in amorphous films $A^{(P)}$, cavity coupling occurred from 0-m ($m=0,1,2$) excitons characteristic of the amorphous phase (Fig. 5(b)), whereas polycrystalline films $F^{(P)}$ exhibited cavity coupling of 0-m ($m=0,1,2,3$) excitons of the crystalline phase (Fig. 5(a)), in spite of the similarity in the bare film optical absorption properties for $F_1^{(B)}$ and $F^{(P)}$ (Fig. 2). (In the crystalline films, the notation ”‘0-m”’ is used to differentiate between different peaks contributing to the absorption spectra in the 1.8-2.4 eV energy region and easier comparison to other films. However, in contrast to dilute blends and amorphous films, the 0-m transitions in crystalline films are not a simple vibronic progression, due to a complicated mixture of various states of Frenkel and CT nature contributing to each peak. [38, 61, 62]) The interaction strength $2V_{00}$ for the amorphous films $A^{(P)}$ of 253 meV was higher than 210 meV for polycrystalline films $F^{(P)}$, as expected from increased molecular density in amorphous films (Fig. 6(b), see Sec. 2.1 and Fig. S3). However, an interesting observation common for amorphous $A^{(P)}$ and polycrystalline $F^{(P)}$ films is that the coupling strength of the oscillators corresponding to 0-m transitions to the cavity does not scale with the square root of the oscillator strength (extracted from fits to the absorption spectra of bare films), which is in stark contrast to observations in TIPS–Pn:PMMA blends $F_1^{(B)}$ and $F_2^{(B)}$ (Fig. 6(a)). This behavior has been previously observed in highly concentrated diF TES-ADT:PMMA blends in similar cavities, [31] data for which are included for comparison in Fig. 6(a), as discussed in the next section.

4 Discussion

The exciton-photon coupling in various film types (Fig. 1) reveals an interesting picture of how the evolving film density and morphology modify the cavity-coupling characteristics in TIPS–Pn-based films. In particular, there are two unexpected observations (Fig. 6):

1. In concentrated TIPS–Pn:PMMA blends (such as$F_1^{(B)}$ or $F_{1.3}^{(B)}$) with both the amorphous and crystalline phases present, the amorphous phase exhibits the strong exciton-photon coupling (Figs. 4 and S12), whereas the crystalline phase does not, even though the optical

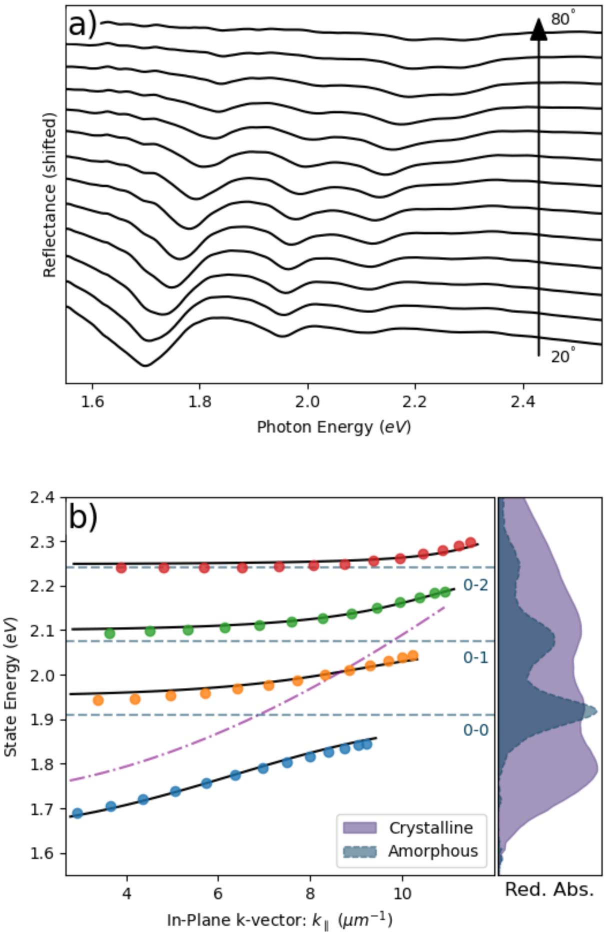

Figure 4: (a) The reflectance from a cavity containing the $F_1^{(B)}$ film at angles of incidence ranging from 20° to 80°. (b) A dispersion plot of the polariton energies extracted from the reflectance. Dots show the experimentally extracted state energy, the dashed-dotted line shows the photon energy, the dashed line shows the exciton energies for amorphous phase and solid black lines show fits according to the coupled oscillator model. Adjacent to (b) is the reduced absorption from the corresponding film (solid line) which shows a crystalline phase response, and the reduced absorption for a $F_2^{(B)}$ film with an amorphous phase response (dashed line) shown for comparison. Notice that the photon is coupled to the amorphous phase in the cavity, despite the absorption spectrum showing a predominately crystalline phase.

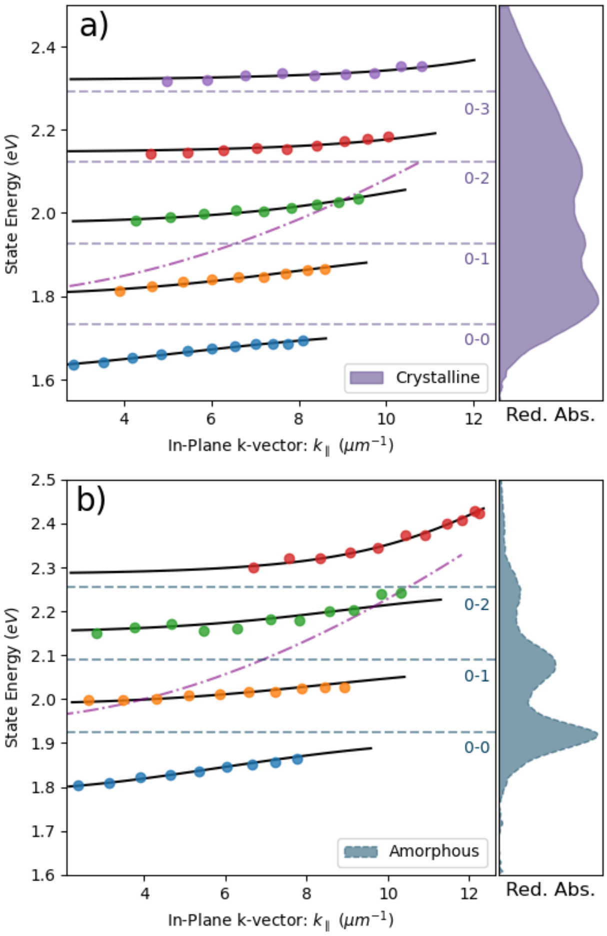

Figure 5: A comparison of the s-polarized polariton dispersions in pristine TIPS–Pn cavities: (a) crystalline film ($F^{(P)}$) cavity with the adjacent reduced absorption of the bare film for comparison and (b) amorphous film ($A^{(P)}$) cavity of comparable to (a) thickness with the adjacent reduced absorption for the bare film shown. For both plots, dots show the experimentally extracted state energies, the dashed-dotted line shows the photon energy, the dashed lines show the exciton energies, and the solid lines show the fits according to the coupled oscillator model. Fit parameter values are given in Tables 1 and S6.

absorption spectra are strongly dominated by those of the crystalline phase (Figs. 2 and S6-S7).

2. The expected scaling of the interaction strength $2V_{0m}$ with the square root of the oscillator strength f_{0m} breaks down in pristine films, both polycrystalline $F^{(P)}$ and amorphous $A^{(P)}$, even though it works well for TIPS–Pn:PMMA blends.

Next, we discuss the possible underlying mechanisms behind these observations.

4.1 Effect of morphology: preferential cavity coupling to amorphous phases

Figure 6(b) illustrates that the coupling between the cavity photon and the lowest-energy exciton described by $2V_{00}$ scales as expected with the square root of the overall molecular density N_{tot} ($2V_{00} \propto \sqrt{N_{tot}} \propto \sqrt{1/\mathcal{V}}$, where $\mathcal{V}$ is the molecular volume, Sec. 2.3 and SI), in spite of differences in the lowest-energy exciton properties in the crystalline and amorphous films seen from Fig. 2.

In order to understand this behavior, we follow Spano's estimate in Ref. [7] that the Rabi splitting in the lowest polariton branch of ~235 meV could be achieved by cavity-coupling of $N_0 = 10^6$ molecules (obtained using the cavity photon energy $\hbar\omega$ of 2 eV, transition dipole moment μ of 10 D, dielectric constant ϵ of 3, and photon mode volume $\mathcal{V}_{\text{mode}}$ of 1 $(\mu m)^3$ in eq 6), which translates into the molecular density $N = N_0/\mathcal{V}_{\text{mode}}$ of $10^{18} cm^{-3}$. As the Rabi splitting in this estimate is in the range of the interaction strengths $2V_{00}$ obtained in pristine TIPS–Pn and diF TES–ADT films ($2V_{00} = 220-340 meV$, Fig. 6(a)), we compare the estimated $N = 10^{18} cm^{-3}$ with the total molecular density N_{tot} of the order of $10^{21} cm^{-3}$ in our pristine films (calculated as described in Sec. 2.3), Fig. 6(b). The comparison suggests that only a small fraction ($\alpha = N/N_{tot} = 10^{-3}$) of all molecules couples to the cavity whereas the rest of the molecules contributes to the reservoir of dark exciton states. [8, 9] Since the $2V_{00}$ coupling energy scales as expected with the overall molecular density N_{tot} (Fig. 6(b)), so that the 0-0 exciton in more dilute films exhibits proportionally lower coupling strengths $2V_{00}$, a similar fraction ($\alpha = 10^{-3}$) of all molecules couples to the cavity in all films, regardless of the molecular concentration.

In terms of existing models, for example using Spano's approach in Refs. [7,8], the observed scaling of $2V_{00}$ with the molecular density in Fig. 6(b) would be presented as $2V_{00} \propto \sqrt{N_{tot}}$ where $N_{tot} = (1/\alpha)(1/\mathcal{V}_{\text{mode}}) \times N_{agg} \times N_M$. Here N_{agg} is the number of resonantly coupled aggregates and N_M is the number of molecules in the aggregate. [8] The data in Fig. 6(b) would indicate that N_{agg} linearly increases with the increased molecular concentration, as it evolves from blend $F_2^{(B)}$ to pristine films $F^{(P)}$ and $A^{(P)}$, while N_M does not change (Fig. 7(a)).

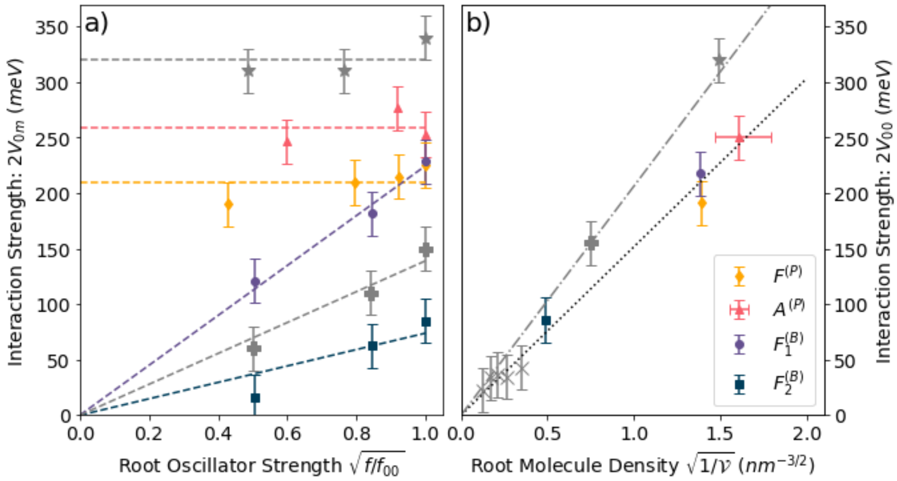

Figure 6: (a) A comparison of the interaction strengths ($2V_{0m}$, $m = 0, 1, 2, 3$) for s-polarized polaritons in each cavity $\left(F_2^{(B)},\ F_1^{(B)},\ F^{(P)},\text{ and } A^{(P)}\right)$ as plotted against the square root of the oscillator strength (relative to the 0-0 exciton) for the associated exciton. For amorphous films $F_2^{(B)}$ and $A^{(P)}$, the oscillator strength is taken as the Franck-Condon (FC) coefficient ($e^{-S}S^m/m!$ where the HR factor S, Table 1). For$F_1^{(B)}$, the oscillator strengths for $F_2^{(B)}$ are used. The dashed lines for each set of data represent either a proportional fit or constant fit to highlight the deviation from a proportional model. The "star" and "plus" markers show comparable data for diF TES–ADT:PMMA blends for crystalline phase (in crystalline P_{agg} films with optical absorption spectra dominated by aggregates) and amorphous phase (in $P_{1.5}$ films with an average diF TES-ADT spacing of 1.5 nm, with contributions from both crystalline and amorphous phases to the optical absorption spectra), respectively. [31] (b) A comparison of the 0-0 interaction strength ($2V_{00}$) for s-polarized polaritons in each cavity type plotted against the square root of the effective molecular density $N_{tot} = 1/\mathcal{V}$ where V is the molecular volume. The dotted line represents a proportional fit, based on equation 10. For $F^{(P)}$, the "molecular density" is estimated from the average crystal axis length, and for $A^{(P)}$ from the estimated film contraction induced by annealing (where horizontal error express bounds of this estimate), see Sec. 2.3 and SI for details. Vertical error bars were estimated at 20 meV based of the coupled oscillators fit. The "star", "plus" and "x" markers show comparable data for 0-0 interaction strength for diF TES–ADT:PMMA in crystalline phase of film P_{agg} ("star") and amorphous phases in films $P_{1.5}$ ("plus"), and P_d with d ranging between 2.5 nm and 6 nm ("x"). [31]

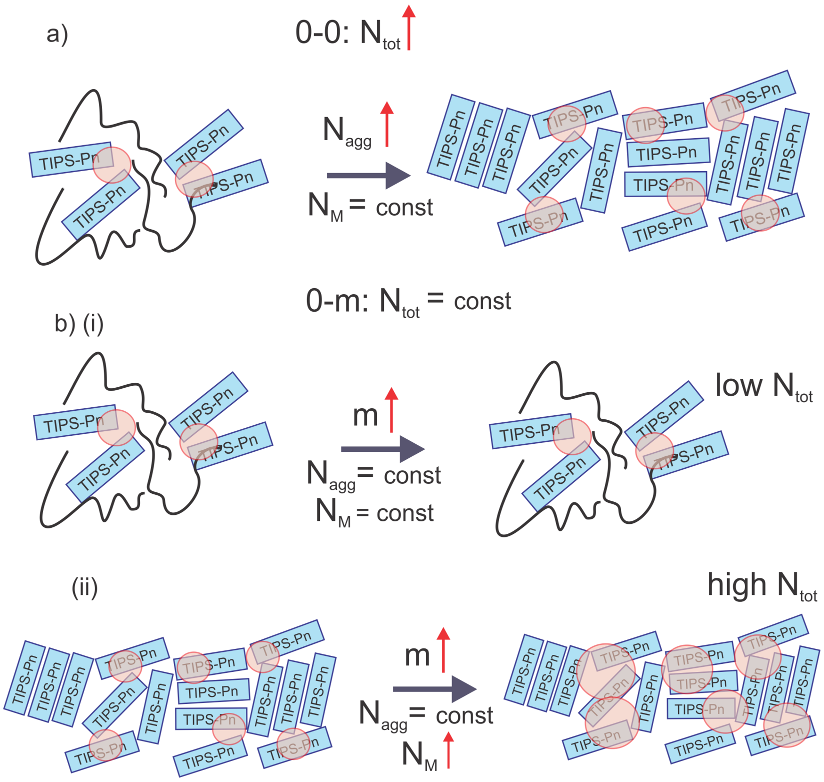

Figure 7: (a) Schematics of how increase in molecular density N_{tot} changes the number of aggregates coupled to the cavity N_{agg} without affecting the delocalization N_M (represented by red circles), for the case of the lowest-energy (0-0) exciton (scenario of Fig. 6(b)). (b): schematics of how the lowest-energy (0-0) and vibrational ($0-m$, $m = 1, 2, ...$) excitons interact with the cavity photon at low (i) and high (ii) molecular density N_{tot} (scenario of Fig. 6(a)). At high molecular density, the interaction strength $2V_{0m}$ increases with m due to an increased exciton delocalization (increased N_M) of the vibrational excitons.

Although the optical absorption spectra and properties of the 0-0 exciton in particular exhibit pronounced differences among films under study, depending on the molecular concentration and morphology (Fig. 1 for TIPS–Pn and Fig. 1 of Ref. [31] for diF TES–ADT), the preserved scaling of $2V_{00}$ with the square root of the overall molecular density N_{tot} (Fig. 6(b)) suggests that a small population of molecules (a fraction α of the N_{tot}) with similar properties, such as molecular arrangements that maximize interactions with the cavity electric field, couples to the cavity in all films, regardless of the macroscopic film morphology and crystallinity. We hypothesize that this population does not rely on long-range crystalline order, but draws from the disordered regions, with properties dominated by those of molecules themselves and nearest-neighbor interactions, instead.

In order to confirm the molecular origin of the cavity-coupled population, we calculated the oscillator strengths for the S_0-S_1 transition for R–Pn and diF R–ADT molecules (where R is a side group, see SI and Table S9) [38] using DFT. The square root of the ratio of the DFT-calculated diF R–ADT and TIPS–Pn oscillator strengths $f_{S_0-S_1}$ of 1.23±0.02, obtained without taking account any intermolecular interactions, is comparable to the ratio of the slopes (1.4±0.1) of the proportional relationship ($2V_{00} \propto \sqrt{N_{tot}}$) obtained from linear fits of the data in Fig. 6(b) for diF TES–ADT and TIPS–Pn (239 ± 9 and 166 ± 8 $meV/nm^{-3/2}$, Table S8).

These estimates are also consistent with our previous observations of $2V_{00} = (271 \pm 11)$ meV (where the $2V_{00}$ value is the average over three cavities of various detunings for s-polarized light) obtained in pristine amorphous films of TIPS–Tc in similar all-metal cavities (e.g. Fig. S14). [30] The R–Tc molecule has a DFT-calculated S_0-S_1 oscillator strength $f_{S_0-S_1}$ in between those for R-Pn and diF R-ADT (Table S9), and the obtained coupling strength $2V_{00}$ of ~270 meV in pristine TIPS–Tc films fits as expected in between the $2V_{00}$ coupling strengths for pristine TIPS–Pn (~220-250 meV for $F^{(P)}$ and $A^{(P)}$) and diF TES–ADT films (~320 meV in P_{agg}) in Fig. 6(b).

The cavity-coupling disordered populations are the dominant type of population for dilute TIPS–Pn:PMMA blends $F_2^{(B)}$ and amorphous films $A^{(P)}$, but they represent a minor, "hidden" population in the crystalline films $F_1^{(B)}$ and $F^{(P)}$. In particular, our procedure for deconvolution of optical absorption spectra, which separates the contributions of the crystalline and amorphous phases to the overall spectra (e.g. Fig. S6 and Table S2 for $F_{1.3}^{(B)}$), did not detect the presence of the amorphous phase in the concentrated TIPS–Pn:PMMA blend $F_1^{(B)}$ (Fig. S7 and Table S3). Yet, the polariton properties indicate that this is the population which couples to the cavity most efficiently in $F_1^{(B)}$ (Fig. 4). Finally, in pristine crystalline films $F^{(P)}$, the LP branch tends to the exciton energy of 1.73 eV at large wave-vectors (Table 1 and Fig. 5(a)), which is 0.04 eV lower than 1.77 eV for the 0-0 peak extracted from the fits of the absorption spectra from the bare films (Table 1 and Fig. S9). This low-energy population could be due to that of defects in the crystallites or at their edges, with short-range interactions close to those of the disordered populations in amorphous films. Similar observations in diF TES–ADT:PMMA films of various diF TES–ADT concentrations [31] suggest that such preferential cavity coupling to disordered populations is not unique for TIPS–Pn and could be a general trend for a variety of acene and ADT materials and beyond. [66]

Extending this logic towards cavity-coupling of single TIPS–Pn crystals with a (00l) orientation similar to that dominant in the polycrystalline films (Fig. S1), but having fewer defects as compared to films, one would expect a lower $2V_{00}$ coupling strength in crystals because of their lower density of disordered molecular populations. Although this hypothesis remains to be proven in single crystals of TIPS–Pn, our explorations of solution-grown diF TES–ADT crystals in all-metal cavities, which exhibit the same brickwork packing motif and the (00l) (l= 1-4) preferential orientation on the substrate as TIPS–Pn, [38,65] support this hypothesis (Fig. S13). In particular, $2V_{00}$ of 120 meV was observed in a diF TES-ADT crystal (Fig. S13), which is lower than 320 meV in high-concentration polycrystalline diF TES-ADT:PMMA blends P_{agg} in Fig. 6(a). [31] However, further investigation is necessary to understand the cavity coupling in films versus single crystals depending on crystal orientations and crystal structure.

4.2 Effect of exciton properties: enhanced cavity coupling of delocalized vibrational excitons

Figure 6(a) illustrates that the TIPS-Pn:PMMA cavities $F_1^{(B)}$ and $F_2^{(B)}$ follow the expected scaling relationship of the coupling strengths V_{0m} for the 0-m exciton transitions with the square root of the 0-m oscillator strength ($2V_{0m} \propto \sqrt{f_{0m}}$), whereas the pristine cavities (both amorphous $A^{(P)}$ and crystalline $F^{(P)}$) do not. This encompasses two interesting observations: (i) it is apparent from the optical absorption and PL spectra of bare films that the properties of the excited states in the amorphous and crystalline phases are considerably different, yet the scaling behavior of $2V_{0m}$ with the oscillator strength is similar in $A^{(P)}$ and $F^{(P)}$. Moreover, optical spectra of bare amorphous pristine films $A^{(P)}$ are considerably more similar to those of the dilute blends $F_2^{(B)}$ than to those of the pristine crystalline films $F^{(P)}$ (Fig. 2). It is curious, then, that the $2V_{0m}$ scaling with f_{0m} in amorphous pristine films $A^{(P)}$ is pronouncedly different from that in the $F_2^{(B)}$ films. What the excited states in pristine films $A^{(P)}$ and $F^{(P)}$ do have in common is a capacity for short-ranged intermolecular interactions of the neighboring molecules with π-π overlap. For example, both the amorphous and crystalline phases exhibit singlet fission [55] mediated by intermolecular interactions, though the process is more efficient in the crystalline phase. (ii) When comparing the lowest-energy (0-0) exciton coupling strengths $2V_{00}$ for films of varying molecular density, TIPS–Pn films follow the scaling relationship ($2V_{00} \propto$

$\sqrt{N_{tot}} \propto \sqrt{1/\mathcal{V}}$) up to and including the pristine films (see Figure 6(b) and Table S8). This indicates that the interaction strength for the lowest-energy exciton in the pristine TIPS–Pn films scales as expected, while the vibrational (0-m, $m > 0$) excitons have a higher than expected interaction strengths (i.e. than what would be predicted by the $2V_{0m} \propto \sqrt{f_{0m}}$ relationship).

What remains to be understood, then, is why the vibrational excitons in the pristine TIPS–Pn cavities have a higher interaction strength than what is expected from the analysis of the oscillator strengths in the optical absorption of bare films. Applying the Spano's model used above, [7, 8] one possible explanation is that the full scaling relationship $2V_{0m} \propto \sqrt{f_{0m}N}$ is still applicable, but that the value of N represents an *effective* number of coupled excitons per mode volume which is larger for the higher-energy excitons (compensating for a lower oscillator strength). In particular, if these excitons are delocalized over a larger number of molecules than the lowest-energy (0-0) exciton, then higher number of molecules would be within the photon's mode volume, increasing the effective molecular density that couples to the cavity photon. With the N_{agg} and N_M notations introduced above, [8] the scenario for the data in pristine TIPS–Pn films in Fig. 6(a) would be represented as $2V_{0m} \propto \sqrt{f_{0m}N}$ where $N = \alpha N_{tot} = (1/\mathcal{V}_{\text{mode}})N_{agg} \times N_M$ with the N_{agg} determined by the molecular density N_{tot} (which is a constant for a film with a given molecular concentration) and N_M increasing with m for 0-m vibrational excitons in pristine TIPS–Pn cavities due to enhanced exciton delocalization (Fig. 7(b)(ii)). This delocalization could either arise directly from larger coherence lengths for the Frenkel exciton states, or indirectly by mixing of the Frenkel excitons with CT states. [38,51,62] In either case, an increased delocalization would require the short-ranged intermolecular interactions of aggregates, and so the dilute TIPS–Pn:PMMA films (such as $F_2^{(B)}$ in Fig. 6(a)) would not exhibit this effect (as schematically shown in Fig. 7(b)(i)) and follow the observed reduced scaling relationship $2V_{0m} \propto \sqrt{f_{0m}}$.

4.3 Effect of local nanomorphology

The breaking of the scaling relationship for pristine TIPS–Pn films is made even more interesting when TIPS–Pn is compared with other (thio)acene-containing cavity systems, in particular diF TES–ADT and TIPS–Tc-based cavities used in our previous work. [30, 31] In the case of diF TES-ADT:PMMA films (discussed in our previous publication [31], c.f. the data included in grey in Figure 6), cavities with mixed crystalline and amorphous phases (the $P_{1.5}$ film, similar to the $F_1^{(B)}$ film here), showed the expected $2V_{0m} \propto \sqrt{f_{0m}}$ scaling relationship while coupling only to the amorphous phase, exactly the scenario observed for the $F_1^{(B)}$ TIPS–Pn:PMMA film. The slope obtained from linear fits of the diF TES–ADT:PMMA film ($P_{1.5}$ in Fig. 6(a)) yielded 140 ± 10 meV. This is in between the slopes of 73 ± 10 meV and 222 ± 10 meV for $F_2^{(B)}$ and $F_1^{(B)}$, as expected based on the molecular densities in these films and the DFT-calculated oscillator strengths $f_{S_0-S_1}$ for the R-Pn and diF R-ADT molecules (Tables S7 and S9). Furthermore, cavities containing highly concentrated crystalline diF TES–ADT:PMMA films (P_{agg}, similar to the $F^{(P)}$ TIPS–Pn film here) exhibited a nearly constant $2V_{0m}$ coupling energy (320 ± 8 meV, Table S7), [31] similar to $F^{(P)}$ cavity (which exhibited a nearly constant coupling energy of 210 ± 7 meV, Table S7).

Interestingly, in contrast to pristine TIPS–Pn and highly-concentrated diF TES–ADT:PMMA films, in pristine amorphous TIPS–Tc films the interaction strength $2V_{0m}$ scaled well with the square root of the oscillator strength (f_{0m}) (Fig. S15)a behavior of dilute TIPS–Pn:PMMA blends such as $F_2^{(B)}$. [30] This raises a question of what is the main origin of differences between the TIPS–Tc films and TIPS–Pn and of similarity between TIPS–Pn and diF TES–ADT films which leads to such drastic differences in the behavior of interaction strengths in TIPS–Tc as compared to TIPS–Pn and diF TES–ADT. A distinguishing feature for TIPS–Tc as compared to TIPS–Pn and diF TES–ADT is its molecular packing motif conducive to forming π-stacked molecular pairs that are arranged in a herringbone geometry (one-dimensional sandwich-herringbone). [67] This is in contrast to TIPS–Pn and diF TES–ADT both of which tend to form a more two-dimensional brickwork structure. [43] We hypothesize that differences in local nanomorphology – driven by the differences in these molecular packing motifs – are behind the differences in $2V_{0m}$ scaling with the oscillator strength f_{0m} in Figs. 6(a) and S15. In this case, even in the absence of the long-range order such as the case of TIPS–Pn amorphous films $A^{(P)}$ and TIPS–Tc amorphous films, the nanoaggregates that couple to the cavity retain molecular packing features similar to those derived from the crystal structure of these materials. For example, the TIPS–Tc molecules would tend to form relatively isolated $\pi - \pi$ stacked dimer pairs (driven by 1D sandwich-herringbone packing tendency), whereas TIPS–Pn would tend to have a larger number of nearest neighbors (driven by 2D brickwork packing tendency). Then, the TIPS–Tc would be expected to exhibit a more localized exciton behavior as compared to TIPS-Pn which would limit the effect of vibrational exciton delocalization (thus, leading to the scenario of Fig. 7(b)(i) as compared to Fig. 7(b)(ii)), discussed above for TIPS–Pn cavities, on the coupling strengths in TIPS–Tc films and exhibit similar scaling with the f_{0m} oscillator strengths for both dilute blends and pristine films. Qualitatively similar observations of the molecular-packing motif-induced differences in exciton delocalization have been previously made in single crystals of diF TSBS-ADT (1D sandwich-herringbone, conducive to localization) versus diF TES-ADT (2D brickwork, conducive to delocalization). [38] Such morphology-driven differences in localization on the molecular level sampled by the cavity coupling of the vibrational excitons translate into the differences in the interaction strength scaling with the "apparent" oscillator strengths (obtained from optical absorption spectra of bare films) highlighting the ability of polariton spectroscopy to reveal not only hidden molecular populations but also their nanoscale-level morphologies.

5 CONCLUSION

In summary, we established how strong exciton-photon coupling evolves in TIPS–Pn-based films placed in all-metal cavities, depending on the molecular density and film morphology. The highest exciton-photon interaction strengths of up to ~$270 meV$ were observed in pristine amorphous TIPS–Pn films, and the interaction strength for the lowest-energy (0-0) exciton scaled with the square root of the molecular density, independent of whether the long-range molecular order was present. The population most strongly coupled to the cavity was revealed to originate from the disordered regions in all films, including pristine crystalline films, with molecular configurations favorable for interacting with the cavity electric field. Such populations are not readily apparent from optical absorption spectra of bare films, which illustrates the capacity of polariton spectroscopy for revealing these hidden ensembles in heterogeneous (mixed-phase) and crystalline films. A break down of the scaling of the exciton-photon interaction strength with the square root of the oscillator strengths for the vibrational excitons, obtained from optical absorption spectra of bare films, was observed in pristine TIPS–Pn films. This observation was attributed to enhanced exciton delocalization of vibrational excitons that relies on short-range intermolecular interactions determined by the molecular packing motif, and in the case of TIPS–Pn, facilitated by the 2D brickwork motif of TIPS–Pn. Similar observations were made for diF TES–ADT films which share the same 2D brickwork packing motif conducive to delocalization, while differing from those in TIPS–Tc films hypothesized to favor a nanomorphology less conducive to delocalization (such as 1D sandwich-herringbone motif observed in crystalline TIPS–Tc). Towards an overarching goal of utilizing the highly coherent nature of polariton states in boosting the performance of organic (opto)electronic devices based on benchmark organic semiconductors under study, our findings have important implications. In particular, since both charge carrier transport and singlet fission rely on the long-range molecular order for achieving best performance, the preferential cavity photon coupling to the molecular population in disordered regions has a potential to mitigate the negative impact of disorder on the device characteristics and relax the requirements of highly ordered systems and achieve enhanced electronic characteristics in disordered strongly-coupled films.

ASSOCIATED CONTENT

Supporting Information: the following files are available free of charge. Details of sample preparation, ellipsometry and XRD characterization of films, optical spectra for various TIPS–Pn-based samples with fits, PL spectra and lifetimes, reflectance spectroscopy data for diF TES–ADT crystals and TIPS–Tc films in all-metal cavities with fits to the coupled oscillators model, fit parameters for various scaling characteristics of the coupling strengths, DFT calculations for R-Pn, diF R-ADT, and R-Tc molecules (PDF)

AUTHOR INFORMATION

Corresponding Author *Email: oksana@science.oregonstate.edu (O.O.)
ORCID
Oksana Ostroverkhova: 0000-0002-3833-161X
John Anthony: 0000-0002-8972-1888

ACKNOWLEDGMENTS

We thank Prof. B. Gibbons for the access to the x-ray diffraction and ellipsometry facilities as well as N. Quist, R. Tollefsen, Dr. K. Tanyi, and Prof. L.-J. Cheng for helpful discussions. This work was supported by the National Science Foundation (DMR-1808258 and CHE-1956431). The fabrication of microcavities was enabled by NSF NNCI:NNI EECS-2025489 award.

ABBREVIATIONS

ADT = anthradithiophene, GW/BSE = GW/Bethe-Salpeter Equation, DFT = density functional theory, LP = lower polariton, PMMA = polymethylmethacrylate, Pn = pentacene, Tc = tetracene, TES = triethylsilylethynyl, TIPS = triisopropylsilylethynyl

References

[1] O. Ostroverkhova “Organic Optoelectronic Materials: Mechanisms and Applications” *Chemical Reviews* (2016) **116**, 13279–13412

[2] O. Ostroverkhova, Ed. “Handbook of Organic Materials for Electronic and Photonic Devices, 2nd Ed.” *Woodhead Publishing* (2018)

[3] J. Keeling and S. Kena-Cohen “Bose-Einstein Condensation of Exciton-Polaritons in Organic Microcavities” *Annual Review of Physical Chemistry* (2020) **71**, 435-459

[4] T. W. Ebbesen “Hybrid LightMatter States in a Molecular and Material Science Perspective” *Accounts of Chemical Research* (2016) **49**, 2403-2412

[5] P. Torma and W. L. Barnes “Strong Coupling Between Surface Plasmon Polaritons and Emitters: a Review” *Reports on Progress in Physics* (2015) **78**, 013901

[6] K. Tanyi, N. Hong, T. Sawyer, J. Van Schenck, G. Giesbers, O. Ostroverkhova, L. J. Cheng “Strong exciton-plasmon coupling in dye-doped film on a planar hyperbolic metamaterial” *Optics Letters* (2020) **45**, 6736

[7] F. Spano “Optical microcavities enhance the exciton coherence length and eliminate vibronic coupling in J-aggregates” *The Journal of Chemical Physics* (2015) **142**, 184707

[8] F. Spano “Excitonphonon polaritons in organic microcavities: Testing a simple ansatz for treating a large number of chromophores” *Journal of Chemical Physics* (2020) **152**, 204113

[9] F. Herrera and J. Owrutsky “Molecular polaritons for controlling chemistry with quantum optics” *Journal of Chemical Physics* (2020) **152**, 100902

[10] R. F. Ribeiro, L. A. Martnez-Martnez, M. Du, J. Campos-Gonzalez-Angulo, and J. Yuen-Zhou “Polariton chemistry: controlling molecular dynamics with optical cavities” *Chemical Science* (2018) **9**, 6325-6339

[11] M. Wei, S. K. Rajendran, H. Ohadi, L. Tropf, M. C. Gather, G. A. Turnbull, and I. D. W. Samuel “Low-threshold polariton lasing in a highly disordered conjugated polymer” *Optica* (2019) **6**, 1124-1129

[12] A. Punitsev, A. Zasedatelev, K. McGhee, T. Cookson, K. Georgiou, D. Sannikov, D. G. Lidzey, and P. G. Lagoudakis “Nano-second exciton-polariton lasing in organic microcavities” *Applied Physics Letters* (2020) **117**, 123302

[13] S. Kena-Cohen and S. Forrest “Room-temperature polariton lasing in an organic single-crystal microcavity” *Nature Photonics* (2010) **4**, 371-375

[14] A. Zasedatelev, A. Baranikov, D. Urbonas, F. Scafirimuto, U. Scherf, T. Stoferle, R. Mahrt, and P. G. Lagoudakis “A room-temperature organic polariton transistor” *Nature Photonics* (2019) **13**, 378-383

[15] G. Lerario, A. Fieramosca, F. Barachati, D. Ballarini, K. Daskalakis, L. Dominici, M. De Giorgi, S. Maier, G. Gigli, S. Kena-Cohen, D. Sanvitto “Room-temperature superfluidity in a polariton condensate” *Nature Physics* (2017) **13**, 837-841

[16] C. Gubbin, S. Maier, and S. Kena-Cohen “Low-voltage polariton electroluminescence from an ultrastrongly coupled organic light-emitting diode” *Applied Physics Letters* (2014) **104**, 233302

[17] E. Eizner, J. Brodeur, F. Barachati, A. Sridharan, S. Kna-Cohen “Organic Photodiodes with an Extended Responsivity using Ultrastrong Light-Matter Coupling” *ACS Photonics* (2018) **13**, 837-841

[18] N. Krainova, A. J. Grede, D. Tsokkou, N. Banerji, and N. C. Giebink “Polaron Photoconductivity in the Weak and Strong Light-Matter Coupling Regime” *Physical Review Letters* (2020) **124**, 177401

[19] M. Wang, M. Hertzog, and K. Borjesson “Polariton-assisted excitation energy channeling in organic heterojunctions” *Nature Communications* (2021) **12**, 1874

[20] V. Nikolis, A. Mischok, B. Siegmund, J. Kublitski, X. Jia, J. Benduhn, U. Hormann, D. Neher, M. Gather, D. Spoltore, and K. Vandewal “Strong light-matter coupling for reduced photon energy losses in organic photovoltaics” *Nature Communications* (2019) **10**, 3706

[21] E. Orgiu, J. George, J. Hutchison, E. Devaux, J. Dayen, B. Doudin, F. Stellacci, C. Genet, J. Schachenmayer, C. Genes, G. Pupillo, P. Samori, T. W. Ebbesen “Conductivity in organic semiconductors hybridized with the vacuum field” *Nature Materials* (2015) **14**, 1123-1129

[22] E. Kang, S. Chen, V. erek, C. Hgglund, E. D. Gowacki, and M. P. Jonsson “Charge transport in phthalocyanine thin-film transistors coupled with FabryPerot cavities” *Journal of Materials Chemistry C* (2021) **9**, 2368-2374

[23] M. Held, A. Graf, Y. Zakharko, P. Chao, L. Tropf, M. Gather, and J. Zaumseil "Ultra-strong Coupling of Electrically Pumped Near-Infrared Exciton-Polaritons in High Mobility Polymers" *Advanced Optical Materials* (2018) **6**, 1700962

[24] D. Coles, N. Somaschi, P. Michetti, C. Clark, P. Lagoudakis, P. Savvidis, and D. G. Lidzey "Polariton-mediated energy transfer between organic dyes in a strongly coupled optical microcavity" *Nature Materials* (2014) **13**, 712-719

[25] B. Liu, P. Rai, J. Grezmak, R. J. Twieg, and K. D. Singer "Coupling of exciton-polaritons in low-Q coupled microcavities beyond the rotating wave approximation" *Physical Review B* (2015) **92**, 155301

[26] C. Cheng, N. Kim, and N. Giebink "Charged Polariton Luminescence from an Organic Semiconductor Microcavity" *ASC Photonics* (2019) **6**, 308-313

[27] M. Slootsky, Y. Zhang, and S. R. Forrest "Temperature dependence of polariton lasing in a crystalline anthracene microcavity" *Physical Review B* (2012) **86**, 045312

[28] D. Polak, R. Jayaprakash, T. P. Lyons, L. . Martnez-Martnez, A. Leventis, K. J. Fallon, H. Coulthard, D. G. Bossanyi, K. Georgiou, A.J. Petty, J. Anthony, H. Bronstein, J. Yuen-Zhou, A. I. Tartakovskii, J. Clark, and A. J. Musser "Manipulating molecules with strong coupling: harvesting triplet excitons in organic exciton microcavities" *Chemical Science* (2020) **11**, 343-354

[29] S. Kena-Cohen and S. R. Forrest "Giant Davydov splitting of the lower polariton branch in a polycrystalline tetracene microcavity" *Physical Review B* (2008) **77**, 073205

[30] R. Puro, J. D. B. Van Schenck, E. Holland, J. E. Anthony, O. Ostroverkhova "Exciton polariton-enhanced photodimerization of functionalized tetracene" *submitted* (2021)

[31] J. Van Schenck, E. K. Tanyi, L.-J. Cheng, J. Anthony and O. Ostroverkhova "Strong exciton-photon coupling in anthradithiophene microcavities: from isolated molecules to aggregates" *MRS Communications* (2019) **9**:3, 956-963

[32] B. Liu, V. Menon, M. Sfeir "Ultrafast thermal modification of strong coupling in an organic microcavity" *APL Photonics* (2021) **6**, 016103

[33] W. E. Moerner and L. Kador "Optical detection and spectroscopy of single molecules in a solid" *Physical Review Letters* (1989) **62**, 2535

[34] W. P. Ambrose, T. Basche, and W. E. Moerner "Detection and spectroscopy of single pentacene molecules in a pterphenyl crystal by means of fluorescence excitation " *Journal of Chemical Physics* (1991) **95**, 7150

[35] M. Orrit and J. Bernard "Single pentacene molecules detected by fluorescence excitation in a p-terphenyl crystal" *Physical Review Letters* (1990) **65**, 2716

[36] W. E. B. Shepherd, R. Grollman, A. Robertson, K. Paudel, R. Hallani, M. A. Loth, J. E. Anthony, and O. Ostroverkhova "Single-molecule imaging of organic semiconductors: Toward nanoscale insights into photophysics and molecular packing" *Chemical Physics Letters* (2015) **629**, 29-35

[37] R. Grollman, N. Quist, A. Robertson, J. Rath, B. Purushothaman, M. M. Haley, J. E. Anthony, and O. Ostroverkhova "Single-molecule insight into nanoscale environment-dependent photophysics in blends" *Journal of Physical Chemistry C* (2017) **121**, 12483-12494

[38] J. Van Schenck, G. Mayonado, J. Anthony, M Graham, and O. Ostroverkhova, “Molecular packing-dependent exciton dynamics in functionalized anthradithiophene derivatives: from solutions to crystals” *Journal of Chemical Physics* (2020) **153**, 164715

[39] O Ostroverkhova, D.G. Cooke, F.A. Hegmann, J.E. Anthony, V. Podzorov, M. E. Gershenson, O. D. Jurschescu and T. T. M. Palstra “Ultrafast carrier dynamics in pentacene, functionalized pentacene, tetracene, and rubrene single crystals” *Applied Physics Letters* (2006) **88**, 162101

[40] N. Hestand, H. Yamagata, B. Xu, D. Sun, Y. Zhong, A. Harutyunyan, G. Chen, H. Dai, Y. Rao, F. C. Spano “Polarized Absorption in Crystalline Pentacene: Theory vs Experiment” *Journal of Physical Chemistry C* (2015) **119**, 22137-22147

[41] J. Johnson “Open questions on the photophysics of ultrafast singlet fission” *Communications in Chemistry* (2021) **4**, 85

[42] C. Cruz, E. Chronister, and C. J. Bardeen “Using temperature dependent fluorescence to evaluate singlet fission pathways in tetracene single crystals ” *Journal of Chemical Physics* (2020) **153**, 234504

[43] J. E. Anthony “The Larger Acenes: Versatile Organic Semiconductors” *Angewandte Chemie International Edition* (2008) **47**, 452-483

[44] Y. Diao, K. Lenn, W. Lee, M. Blood-Forsythe, J. Xu, Y. Mao, Y. Kim, J. A. Reinspach, S. Park, A. Aspuru-Guzik, G. Xue, P. Clancy, Z. Bao, and S. C. B. Mannsfeld “Understanding Polymorphism in Organic Semiconductor Thin Films through Nanoconfinement” *Journal of the American Chemical Society* (2014) **136**, 17046-17057

[45] O Ostroverkhova, D.G. Cooke, S. Shcherbyna, R. Egerton, R. R. Tykwinski, J. E. Anthony, F.A. Hegmann “Band-like transport in pentacene and functionalized pentacene thin films revealed by sub-picosecond transient photoconductivity measurements” *Physical Review B* (2005) **71**, 035204

[46] G. Giri, S. Park, M. Vosgueritchian, M. Shulaker, Z. Bao “High-Mobility, Aligned Crystalline Domains of TIPS-Pentacene with Metastable Polymorphs Through Lateral Confinement of Crystal Growth” *Advanced Materials* (2014) **26**, 487-493

[47] D.Kneppe, F.Talnack, B.K.Boroujeni, C.Teixeir da Rocha, M.Hppner, A.Tahn, S.C.B.Mannsfeld, F.Ellinger, K.Leo, H.Kleemann “Solution-processed pseudo-vertical organic transistors based on TIPS-pentacene” *Materials Today Energy* (2021) **21**, 100697

[48] O. Ostroverkhova, S. Shcherbyna, D. Cooke, R. Egerton, and F. Hegmann “Optical and transient photoconductive properties of pentacene and functionalized pentacene thin films: Dependence on film morphology” *Journal of Applied Physics* (2005) **98**, 033701

[49] J. E. Anthony, J. S. Brooks, D. L. Eaton, and S. R. Parkin “Functionalized Pentacene: Improved Electronic Properties from Control of Solid-State Order” *Journal of the American Chemical Society* (2001) **123**(38), 9482-9483

[50] A. Jones, N. Kearns, J. Ho, J. Flach, M. Zanni “Impact of non-equilibrium molecular packings on singlet fission in microcrystals observed using 2D white-light microscopy” *Nature Chemistry* (2020) **12**, 40-47

[51] C. Wong, B. Cotts, H. Wu, N. Ginsberg “Exciton dynamics reveal aggregates with intermolecular order at hidden interfaces in solution-cast organic semiconducting films” *Nature Communications* (2015) **6**, 5946

[52] B. Walker, A. Musser, D. Beljonne, and R. H. Friend "Singlet exciton fission in solution" *Nature Chemistry* (2013) **5**, 1019-1024

[53] L. Yang, M. Tabachnyk, S. L. Bayliss, M. L. Bhm, K. Broch, N. C. Greenham, R. H. Friend, and B. Ehrler "Solution-Processable Singlet Fission Photovoltaic Devices" *Nano Letters* (2015) **15**, 354-358

[54] C. Grieco, G. S. Doucette, K. T. Munson, J. R. Swartzfager, J. M. Munro, J. E. Anthony, I. Dabo, and John B. Asbury "Vibrational probe of the origin of singlet exciton fission in TIPS-pentacene solutions" *Journal of Chemical Physics* (2019) **151**, 154701

[55] K. T. Munson, J. Gan, C. Grieco, G. S. Doucette, J. E. Anthony, and J. B. Asbury "Ultrafast Triplet Pair Separation and Triplet Trapping following Singlet Fission in Amorphous Pentacene Films" *The Journal of Physical Chemistry C* (2020) **124**(43), 23567–23578

[56] S. Sharifzadeh, C. Wong, H. Wu, B. Cotts, L. Kronik, N. Ginsberg, and J. B. Neaton "Relating the Physical Structure and Optoelectronic Function of Crystalline TIPS-Pentacene" *Advanced Functional Materials* 2015 **116**, 2038-2046

[57] B. Liu, V. Menon, M. Sfeir "The Role of Long-Lived Excitons in the Dynamics of Strongly Coupled Molecular Polaritons" *ACS Photonics* (2020) **7**, 2292-2301

[58] W. E. Moerner and M. Orrit "Illuminating Single Molecules in Condensed Matter" *Science* (1999) **283**, 1670-1676

[59] H. Yamagata, D. Maxwell, J. Fan, K. Kittilstved, A. Briseno, M. Barnes, F. C. Spano, *J. Phys. Chem. C* (2014) **118**, 28842

[60] M. Fox "Quantum Optics: An Introduction" *Oxford University Press* (2005)

[61] D. James ,J. Frost, J. Wade, J. Nelson, J. Kim "Controlling Microstructure of Pentacene Derivatives by Solution Processing: Impact of Structural Anisotropy on Optoelectronic Properties" *ACS Nano* (2013) **7**, 7983-7991

[62] Y. Li, J. Wan, D. Smilgies, R. Miller, R. Headrick "Enhancement of charge transfer in thermally-expanded and strain-stabilized TIPS-pentacene thin films" *Phys. Rev. Res* (2020) **2**, 033294

[63] W. Shepherd, A. Platt, D. Hofer, O. Ostroverkhova, M. Loth, J. Anthony, "Aggregate formation and its effect on (opto)electronic properties of guest-host organic semiconductors" *Appl. Phys. Lett.* (2010) **97**, 163303

[64] N. Hestand and F. C. Spano "Expanded Theory of H- and J-Molecular Aggregates: The Effects of Vibronic Coupling and Intermolecular Charge Transfer" *Chemical Reviews* 2018 **118**, 7069-7163

[65] K. Paudel, G. Giesbers, J. Van Schenck, J. E. Anthony, and O. Ostroverkhova "Molecular packing-dependent photoconductivity in functionalized anthradithiophene crystals" *Organic Electronics* (2019) **67**, 311-319

[66] F. Le Roux and D. D. C. Bradley "Conformational control of exciton-polariton physics in metal-poly(9,9-dioctylfluorene)-metal cavities" *Physical Review B* (2018) **98**, 195306

[67] H. Stern, A. Cheminal, S.R. Yost, K. Broch, S. Bayliss, K. Chen, M. Tabachnyk, K. Thorley, N. Greenham, J. Hodgkiss, J. Anthony, M. Head-Gordon, A. Musser, A. Rao, and R. H. Friend "Vibronically coherent ultrafast triplet-pair formation and subsequent thermally activated dissociation control efficient endothermic singlet fission" *Nature Chemistry* (2017) **9**, 1205-1212